

Mapping molecular polariton transport via pump-probe microscopy

Piper Fowler-Wright,¹ Michael Reitz,¹ and Joel Yuen-Zhou¹

¹*Department of Chemistry and Biochemistry, University of California San Diego, La Jolla, California 92093, USA*
(Dated: April 23, 2025)

We demonstrate how the transport properties of molecular polaritons in optical cavities can be extracted from a microscopic modeling of pump-probe spectroscopy. Our approach combines a mean-field treatment of the light-matter Hamiltonian with a perturbative expansion of both light and matter components, along with spatial coarse-graining. This approach extends semiclassical cavity spectroscopy to multimode light-matter interactions, providing full access to spatially-resolved transport spectra. By simulating a microscopy experiment with counter-propagating pump and probe pulses, we compute the differential transmission and show how molecular dephasing and persistent dark exciton populations drive sub-group-velocity transport of the root-mean-square displacement. We analyze transport across the polariton dispersion, showing how velocity renormalization correlates with excitonic weight, consistent with experimental observations, and further its dependence on the rate of molecular dephasing. Our results highlight the need to consider measured spectroscopic observables when characterizing transport in polaritonic systems.

Exciton polaritons are hybrid light-matter quasiparticles formed through strong coupling of confined electromagnetic modes with electronic excitations. Their photonic component allows them to travel ballistically with a small effective mass, enabling efficient, long-range energy transport that may be exploited in novel optoelectronic devices [1–3]. Molecular materials such as organic dye films offer a particularly promising platform for this purpose, on account of the ease and flexibility of their fabrication, and operability at room temperatures [4].

Recent advancements in ultrafast nonlinear spectroscopic techniques have enabled imaging of molecular polariton transport on sub-picosecond timescales in a range of closed and open cavity structures [5–13]. Surprisingly, these experiments report not simply ballistic transport at the polariton group velocity, but transport velocities renormalized according to the excitonic content of the propagating excitation, and, ultimately, a crossover to diffusive behavior. These results have prompted extensive research [14–25] into the mechanism of transport of hybrid light-matter states in molecular systems and, in particular, the role of dark exciton states in the dynamics [26].

A large number of approaches have been taken to model molecular polariton transport, ranging from kinetic models of thermally-activated scattering [6] to mixed quantum-classical treatments [11, 27] and molecular dynamics simulations [14, 17, 18]. While these models capture different aspects of the transport, they do so by characterizing individual photon, molecular, or polariton populations—quantities that may not directly correspond to experimental observables: in the time-resolved technique of pump-probe microscopy, transient signals are often collected without regard as to their specific origin, polaritonic or otherwise [26, 28]. A more complete interpretation thus requires understanding how different excitations contribute to the observed spectroscopic signal.

In this Letter, we present a microscopic model of a pump-probe transport experiment in an organic microcavity (Fig. 1(a)). Our method extends the framework for nonlinear cavity spectroscopy introduced in Ref. [29], which is based on a perturbative expansion of both light and matter components of the system, to multimode configurations. This allows us to gain insight into the different contributions to spectroscopic signals in a space- and time-resolved manner. We apply this method to show how sub-group-velocity transport, as extracted from the root-mean-square displacement, emerges in a simple model of molecular polariton transport with pure dephasing. In particular, we assess the role of dark excitonic populations in renormalizing the velocity and the dependence of transport properties on in-plane cavity momentum and dephasing rate.

Model.—We consider N molecules as a collection of two-level systems (Pauli matrices σ_i^α) interacting with N_k modes of a microcavity (bosonic annihilation operators a_k) according to the Tavis–Cummings (TC) Hamiltonian under the rotating-wave approximation. Setting $\hbar = 1$,

$$H = \sum_{k=1}^{N_k} \omega_k a_k^\dagger a_k + \sum_{n=1}^N \frac{\omega_0}{2} \sigma_n^z + \sum_{k=1}^{N_k} \sum_{n=1}^N g(a_k \sigma_n^+ e^{ikr_n} + \text{H.c.}), \quad (1)$$

where ω_0 is the molecular transition frequency, g the light-matter coupling strength of a single molecule, and ω_k describes the cavity dispersion.

For simplicity, we consider a 1D chain where the N molecules are distributed between N_k sites, and a quadratic dispersion $\omega_k = \omega_c + k^2 c^2 / 2\omega_c$, which approximates the dispersion of a planar microcavity [30]. Here, k is the in-plane momentum, quantized as $k = 2\pi Q/L$ with $Q = -N_k/2, \dots, N_k/2$ and system length L ; N_k is chosen such that $\Delta r = L/N_k$ provides adequate spatial

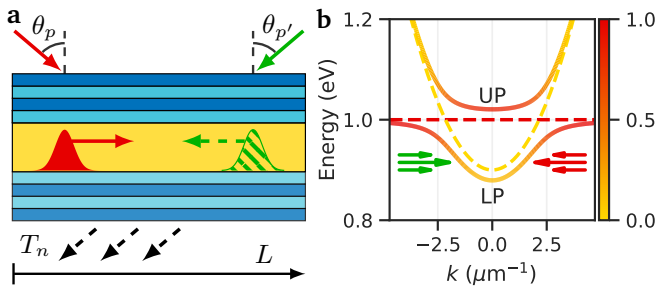


FIG. 1. *Schematics.* (a) A planar microcavity of extent L is driven by counter-propagating pump (p) and probe (p') fields impinging at $\theta_{p,p'}$. The pump generates laterally-propagating light-matter wavepackets probed by the p' field. Information of pump-induced transport is retrieved through the spatially-resolved transmitted field T_n detected along the probe direction. (b) Polariton dispersions versus in-plane momentum k . The color scale indicates the excitonic fraction X_k^2 of the upper (UP) and lower (LP) polariton branches and the bare cavity dispersion and exciton energy are shown as dashed lines. Arrows indicate resonant excitation of LP by the pump and probe pulses centered at $k_{p,p'} = \pm\pi/2 \mu\text{m}^{-1}$.

resolution. The cavity frequency ω_c is set by the normal wavevector component, $k_\perp = \omega_c/c$, in turn fixed by the resonance condition of the relevant longitudinal cavity mode. While we assume identical molecules, i.e., uniform ω_0 and g , the numerical pump-probe spectra calculations presented below can be readily extended to include energetic disorder and inhomogeneous couplings.

Explicit expressions for the eigenstates of Eq. (1) may be derived for low excitation densities [31]. At each k , the system supports two bright eigenstates, the upper (UP, +) and lower (LP, -) polaritons, with frequencies

$$\omega_k^{\text{UP/LP}} = \frac{1}{2} \left[\omega_0 + \omega_k \pm \sqrt{(\omega_0 - \omega_k)^2 + 4\Omega^2} \right]. \quad (2)$$

Here $\Omega = g\sqrt{N}$ represents the collective light-matter coupling, yielding a splitting of 2Ω at resonance.

The frequencies $\omega_k^{\text{UP/LP}}$ are plotted alongside the cavity dispersion and exciton frequency in Fig. 1(b). Importantly, the group velocity $v_k^{\text{grp}} = \partial_k \omega_k^{\text{LP}}$ provides a theoretical reference for comparing with the observed velocities in our simulations following LP excitation. Additionally, the excitonic fraction X_k^2 of the eigenstates, shown as a color scale in Fig. 1(b), will be useful to connect excitation composition to transport properties. Broadly, as X_k^2 increases with $k > 0$ along the lower polariton branch, one expects more matter-like, i.e., slowly diffusive, behavior.

After the polaritons, the remaining degrees of freedom comprise asymmetric molecular combinations at the transition frequency ω_0 that are optically dark [26]. As we explain below, the population of these dark exciton states, which are stationary (or slowly diffusing), is crit-

ical to the observed transport.

In addition to the unitary dynamics generated by Eq. (1), we consider decay at rate κ from each cavity mode and dephasing γ_ϕ of the molecules. These are included as Markovian loss terms in the master equation for the total density operator ρ ,

$$\partial_t \rho = -i[H, \rho] + \sum_{k=1}^{N_k} \kappa \mathcal{L}[a_k] + \sum_{n=1}^N \gamma_\phi \mathcal{L}[\sigma_n^z], \quad (3)$$

with $\mathcal{L}[x] = x\rho x^\dagger - \{x^\dagger x, \rho\}/2$. More complex models of molecular and photonic environments may also be incorporated with our approach (see Conclusion & outlook).

Mean-field approach.—To solve the model described by Eq. (3), we apply a mean-field approximation, which assumes that the density operator ρ has a product form. Expectation values involving photonic and molecular operators can then be factorized, e.g., $\langle a_k \sigma_n^z \rangle \approx \langle a_k \rangle \langle \sigma_n^z \rangle$. This ansatz is exact for the TC model in the limit $N \rightarrow \infty$ [32] and produces a closed set of Heisenberg equations of motion for the operators $\langle a_k \rangle$, $\langle \sigma_n^- \rangle$ and $\langle \sigma_n^z \rangle$. The number of equations scales with the number of chain positions N_k , with $N_k \sim 10^2$ for micrometer resolution for the system length $L = 200 \mu\text{m}$ we consider. Deviation from mean-field behavior may occur when cavity vacuum fluctuations become relevant, e.g., in spontaneous photoluminescence measurements [33]. However, we do not expect these processes to be important for the nonlinear microscopy signals of interest.

Introducing the transform $a_n = (1/\sqrt{N_k}) \sum_k e^{ikr_n} a_k$ of the photon operators, the mean-field equations can be cast in real space as

$$\partial_t \langle \tilde{a}_n \rangle = -(i\omega_c + \kappa/2) \langle \tilde{a}_n \rangle - i\Omega \langle \sigma_n^- \rangle + iC \partial_n^2 \langle \tilde{a}_n \rangle + \sqrt{\kappa} \langle \tilde{a}_n^{\text{in}} \rangle, \quad (4a)$$

$$\partial_t \langle \sigma_n^- \rangle = -(i\omega_0 + \gamma_\phi/2) \langle \sigma_n^- \rangle + i\Omega \langle \sigma_n^z \rangle \langle \tilde{a}_n \rangle, \quad (4b)$$

$$\partial_t \langle \sigma_n^z \rangle = -4\Omega \text{Im} [\langle \sigma_n^- \rangle \langle \tilde{a}_n \rangle^*], \quad (4c)$$

where $C = c^2/(2\omega_c \Delta r^2)$, and we defined the rescaled photon variables $\tilde{a}_n = \sqrt{N_k/N} a_n$, such that the equations do not depend explicitly on N . The input field $\langle \tilde{a}_n^{\text{in}} \rangle$ is defined further below.

The mean-field approach with coarse-graining provides an efficient way of computing the spatially-resolved dynamics of microcavity systems with large numbers of molecules, without restriction to the first-excitation manifold. Next, we explain how the method can be integrated with the perturbative nonlinear spectroscopy framework of Ref. [29] to compute spatially-resolved pump-probe spectra.

In pump-probe microscopy experiments, two excitation schemes are commonly used [11, 26]. In the first, non-resonant pump at high energies creates a reservoir of electronic excitations that scatter and populate the polariton branches indiscriminately to a large degree. A

probe pulse is then tuned to a target energy and momentum. In the second, the pump is itself tuned to a specific point on the polariton dispersion, generating coherent polariton populations. This second, resonant excitation scheme, can be more naturally incorporated in the mean-field approach.

Pump and probe pulses are included as driving terms for the photonic variable $\langle \tilde{a}_n \rangle$ in Eq. (4a), by setting

$$\sqrt{\kappa} \langle \tilde{a}_n^{\text{in}}(t) \rangle = \eta_p f_p(t) e^{i\omega_p t} D_n^p + \eta_{p'} f_{p'}(t) e^{i\omega_{p'} t} D_n^{p'}. \quad (5)$$

Here, η_β , $f_\beta(t)$ and ω_β define the amplitude, temporal pulse shape and frequency of the pump ($\beta = p$) and probe ($\beta = p'$), while D_n^β specifies their spatial profiles. The profiles include a modulation $\sim e^{ik_\beta r_n}$ at the central pump and probe wavevectors, which we initially set to $k_p = -k_{p'} = \pi/2 \mu\text{m}^{-1}$.

Below, we consider Gaussian pulses of temporal width $\sigma_t = 25$ fs and spatial width $\sigma_r = 5 \mu\text{m}$ centered in energy on the lower polariton frequency at the target momenta, $\omega_p = \omega_{p'} = \omega_{k_p}^{\text{LP}}$.

Pump-only dynamics.—Before analyzing the spectroscopic signal observed in pump-probe experiments, we examine pump-only dynamics, i.e., $\eta_{p'} = 0$, which provide insight into the role of dark populations in transport.

Dynamics following resonant excitation of the LP branch at $k_p = \pi/2 \mu\text{m}^{-1}$ are shown in Fig. 2. We examine both the photon population n^{ph} and exciton population n^{m} as functions of position, for molecular dephasing $\gamma_\phi = 0$ and $\gamma_\phi = \kappa/2$.

First, in the absence of dephasing (Figs. 2(a) and 2(b)), there is no decoherence, and n^{ph} is depleted solely by cavity decay κ , while n^{m} exhibits a transient signal that mirrors n^{ph} , i.e., follows the polariton. Both populations propagate at the expected group velocity $v_{k_p}^{\text{grp}}$, as may be verified by calculating their mean or root-mean-square (rms) displacement from the initial pump spot $r_n = 0$.

Introducing dephasing (Figs. 2(c) and 2(d)) significantly alters the dynamics. The cavity population n^{ph} depletes more rapidly, as the total linewidth is determined by both κ and γ_ϕ . In particular, transfer to incoherent dark exciton states occurs at rate γ_ϕ , as discussed further below.

As a result, a “dragged” molecular population n^{m} appears from the passing polariton wavepacket, as local incoherent excitons are created but remain stationary [9, 10]. Crucially, when considering both coherent and incoherent populations, the rms displacement propagates with sub-group-velocity. As the polariton signal diminishes, one ultimately expects a transition to a diffusive regime, although exciton hopping is not included in our model.

In Figs. 2(a) and 2(c), we also plot an analytical prediction for the decay of the polariton—and so photon—population with position, derived from the mean-field equations in the linear regime (see End Matter): given

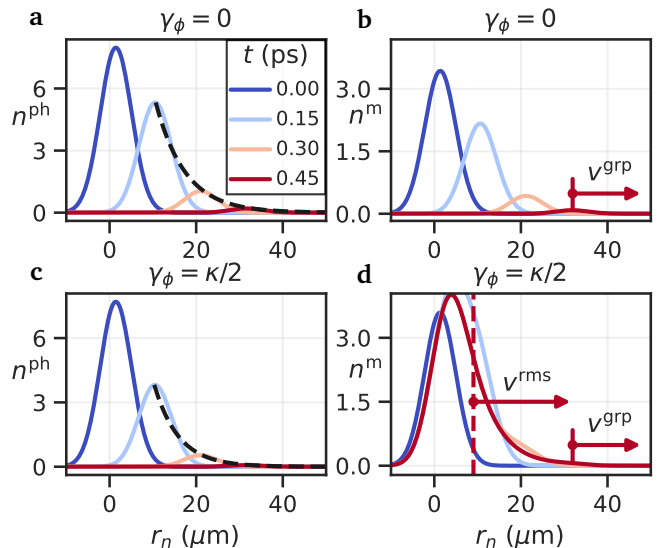


FIG. 2. *Pump-induced population dynamics.* Dynamics of total (a) photon and (b) molecular populations in the absence of dephasing ($\gamma_\phi = 0$). (c), (d) Corresponding dynamics when dephasing is introduced ($\gamma_\phi = \kappa/2$). In (d), the rms deviation at $t = 0.45$ ps is shown with a dashed vertical line whilst the solid line indicates the coherent part moving at the LP group velocity. Black dashed curves in (a) and (c) show the result from Eq. (6) with $\omega_{k_0}^L \approx 0.922$ eV, $k_p = \pi/2 \mu\text{m}^{-1}$, starting from the peak at $t = 0.15$ ps. Parameter values used for all figures were, in units relative to $\omega_0 = 1$ eV, $\omega_c = 0.9$, $\Omega = 0.05$ and $\kappa = 0.01$. We set $N_k = 601$ positions for a chain of length $L = 200 \mu\text{m}$ and $N = 10^6$ molecules.

the population $n_{n_0}^{\text{ph}}$ at site n_0 (position r_{n_0}),

$$n_n^{\text{ph}} = n_{n_0}^{\text{ph}} e^{\lambda(\omega_{k_0}^L)|n-n_0|}, \quad (6)$$

where

$$\lambda^2(\omega) = -\frac{1}{C} [(\omega - \omega_c) + i\kappa/2 + \Omega^2 \chi(\omega)], \quad (7)$$

with $\chi(\omega)$ denoting the linear molecular susceptibility.

We note λ^2 is proportional to the inverse retarded photon Green’s function $D^R(\omega)$ [34]. Hence, $D^R(\omega)$ serves an important figure of merit for lateral transport within a cavity, providing a characteristic length scale over which excitations can propagate. Eq. (6) can be regarded as a version of the famous Beer-Lambert law for lateral polariton transport [35].

Bright & dark state dynamics.—The role of molecular dephasing in transfer to the dark manifold becomes evident from the rate equations for the bright (p^B) and dark (p^D) populations, which follow from Eqs. (4b) and (4c) (see End Matter):

$$\partial_t p_n^B = -\gamma_\phi p_n^B - 2\Omega \text{Im} \Pi_n \cdot (1 - 2p_n^{\text{m}}), \quad (8a)$$

$$\partial_t p_n^D = +\gamma_\phi p_n^B - 2\Omega \text{Im} \Pi_n \cdot 2p_n^{\text{m}}. \quad (8b)$$

Here, $p_n^m(t) = n_n^m/N_E = (1 + \langle \sigma_n^z \rangle)/2$ is the molecular population per molecule at site n , i.e., the excitation probability, and $\text{Im} \Pi_n(t) = \text{Im}(\langle a_n \rangle \langle \sigma_n^+ \rangle)$ represents light-matter correlations. These correlations act as a source in both equations, though for p^D , the contribution is suppressed at typical excitation densities $p^m \ll 1$.

Thus, bright states directly feed dark states at a rate γ_ϕ , leading to the behavior seen in Fig. 2(d). Notably, phase information is lost during scattering into dark states, making this bulk incoherent transfer irreversible in the absence of vacuum fluctuations (e.g., radiative pumping or vibrationally-assisted scattering [36]). This aligns with recent insights into molecular polariton dynamics [37, 38]: transitions from dark states back to polariton states occur via single light-matter coupling $g \propto 1/\sqrt{N}$ [39–41] and are therefore suppressed as $N \rightarrow \infty$.

Pump-probe spectroscopy.—Following Ref. [29], we expand all quantities in pump (p) and probe (p') strength,

$$\begin{aligned} \langle a_n \rangle &= \sum_{a,b} \eta_p^a \eta_{p'}^b \alpha_n^{(a,b)}, \\ \langle \sigma_n^- \rangle &= \sum_{a,b} \eta_p^a \eta_{p'}^b s_n^{(a,b)}, \quad \langle \sigma_n^z \rangle = \sum_{a,b} \eta_p^a \eta_{p'}^b z_n^{(a,b)}. \end{aligned} \quad (9)$$

Substituting into the mean-field equations Eqs. (4a) to (4c), we obtain a hierarchical system of equations for the coefficients $\alpha_n^{(a,b)}$, $s_n^{(a,b)}$, and $z_n^{(a,b)}$, detailed in the End Matter.

We now identify an appropriate spectroscopic observable. Since pump-probe experiments are inherently nonlinear optical measurements, they capture differential signals—specifically, the change in cavity output between pump-on and pump-off conditions. Accordingly, we consider the differential transmission, $\Delta T = T^{p\text{-on}} - T^{p\text{-off}}$.

As explained in Ref. [29], the lowest-order contribution to ΔT arises from the combination of the first-order probe and second-order pump cavity fields, $\Delta T(\omega) \sim \alpha^{(0,1)}(\omega) \bar{\alpha}^{(2,1)}(\omega)$, where an overline denotes complex conjugation. Extending this to the multimode model, we define the position-dependent differential transmission

$$\Delta T_n(\omega) = (\kappa^2/2) \text{Re}[\alpha_n^{(0,1)}(\omega) \bar{\alpha}_n^{(2,1)}(\omega)]. \quad (10)$$

In words, this expression constitutes the heterodyning of the third-order signal $\alpha_n^{(2,1)}$ by the probe $\alpha_n^{(0,1)}$. The setup with counter-propagating pulses provides a simple way to separate out pump and probe signals, which is a practical challenge in experiments. Figure 3 shows $\Delta T_n(\omega)$ following pump ($r_n = -50 \mu\text{m}$) and probe ($r_n = 50 \mu\text{m}$) pulses initiated at either side of the cavity with opposite momenta, $k_p = -k_{p'} = \pi/2 \mu\text{m}^{-1}$. The signal is plotted for four probe delays $\Delta\tau$, where $\Delta\tau = 0$ corresponds to the pump and probe pulses meeting at the center of the cavity. The direct calculation of a physical observable for imaging experiments in Eq. (10) is a main advancement of our work.

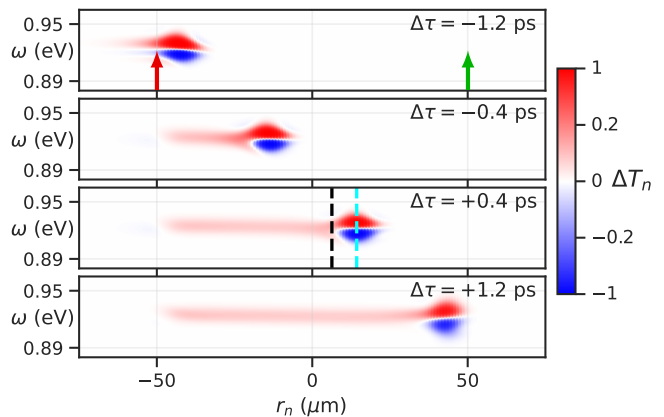


FIG. 3. *Spatiotemporal pump-probe spectra.* Differential transmission ΔT_n following evolution of a LP wavepacket. In the top panel, arrows indicate the spatial positions of the pump (red) and probe (green) spots. In the third panel, the black dashed line indicates the rms width of the polariton distribution, while the cyan line marks the center (maximum) of the polariton wavepacket. A nonlinear colorbar scaling was used to aid visibility of the trailing red feature. A movie of the full dynamics is provided as Supplementary Material [42].

The leading circular feature in each panel of Fig. 3 is the coherent excitation, i.e., the polariton, with red-blue lobes resulting from Rabi contraction following blue shift of the LP [29, 43]. Tracking the position of this feature, determined approximately by the maximum of the absolute signal (cyan line in third panel of Fig. 3), we find the calculated velocity is close to the theoretical group velocity $v_{k_p}^{\text{grp}}$ from the dispersion curve (Fig. 4(a)).

In addition, a trailing feature in ΔT_n emerges, corresponding to the population of static dark excitonic states. Consequently, the rms displacement of the entire signal, which is often reported in experiments, propagates significantly below $v_{k_p}^{\text{grp}}$, as shown in Fig. 4(a). We note that the situation in a real experiment [11] is likely more complex than the picture presented here, i.e., one might not observe a clear distinction between incoherent and coherent parts of the signal. We comment on appropriate extensions to our model below.

Next, we repeat the simulation for different pump-probe momenta $|k_p| = |k_{p'}|$. Extracting the rms velocity $v_{k_p}^{\text{rms}}$ in each case, we find the velocity renormalization to increase with exciton content, Fig. 4(b), as has been frequently reported in experiments [5–13]. We further show how increasing γ_ϕ at fixed pump-probe momenta also increases the renormalization (red dots in Figs. 4(a) and 4(c)). Both trends align with our explanation of sub-group-velocity transport due to stationary dark excitons, since the feeding of these populations is set by both the molecular fraction of the polariton, p^B , and the dephasing rate γ_ϕ . Conversely, we expect decreasing κ to protect the fraction of the propagating exciton that is polariton, hence reduce the velocity renormalization, in

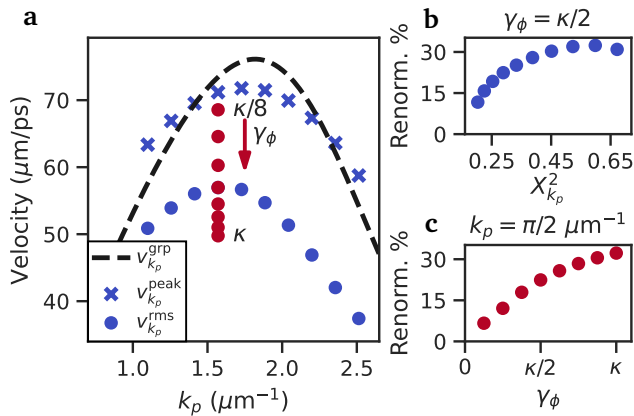


FIG. 4. *Transport renormalization.* (a) Blue: velocity of the circular feature ($v_{k_p}^{\text{peak}}$, crosses) and rms displacement ($v_{k_p}^{\text{rms}}$, circles) for various pump wave vectors k_p at $\gamma_\phi = \kappa/2$. The velocities were calculated from a straight line fit to the position of the maximum and rms displacement of $|\Delta T_n|$ over many delays $-0.8 \text{ ps} \leq \Delta\tau \leq 0.8 \text{ ps}$. The dashed curve shows the theoretical group velocity $v_{k_p}^{\text{grp}}$. (b) Increasing renormalization $v_{k_p}^{\text{rms}}/v_{k_p}^{\text{grp}}$ is observed with increasing k_p and so excitation fraction $X_{k_p}^2$. (a), Red: $v_{k_p}^{\text{rms}}$ at $k_p = \pi/2 \mu\text{m}^{-1}$ and γ_ϕ increasing from $\kappa/8$ to κ in increments of $\kappa/8$. The corresponding renormalization trend is shown in (c).

line with observed trends versus cavity Q -factor [10, 18].

Conclusion & outlook.—We developed a framework for molecular polariton transport in multimode cavities by calculating spatiotemporally-resolved spectra, providing a clear understanding of how dark excitonic populations can renormalize the transport properties in a simplified model of a pump-probe experiment. By analyzing the nonlinear differential transmission, we demonstrated how irreversible transfer to dark exciton states, induced by molecular dephasing, creates stationary excitonic populations that slow net transport. Moreover, that this renormalization becomes more pronounced with increased excitonic weight X_k^2 and molecular dephasing γ_ϕ . Similar dependence on X_k^2 has been widely reported in experiments, while that on γ_ϕ could be investigated, e.g., using materials with different electron-phonon coupling strengths.

We considered the lowest-order nonlinear signal for a counter-propagating pump-probe experimental setup, which has the advantage of providing clear separation of the pump and probe signals. While we used a simple model of pure dephasing for molecular emitters, our approach readily extends to multi-level systems, including coupling to vibrational modes directly [44]. An accurate description of vibronic coupling may be essential for a complete understanding of real experiments where these interactions dominate the dynamics [11]. Furthermore, this method could be applied to calculate higher-order nonlinear responses and explore alternative experimen-

tal schemes not limited to microcavity exciton-polaritons. For example, one may consider setups involving local probe fields that are scanned to construct a real-space image [12].

Future work may also incorporate higher-order correlations beyond the mean-field description to understand analogous microscopy experiments based on photoluminescence measurements [45], or integrate our approach with FDTD electromagnetic simulations [20, 46] to account for arbitrary photonic environments.

Acknowledgements.—This research was primarily supported by the Air Force Office of Scientific Research (AFOSR) through the Multi-University Research Initiative (MURI) program no. FA9550-22-1-0317. We acknowledge helpful discussion with Milan Delor, Yongseok Hong and Harsh Bhakta. P. F.-W. thanks Jonathan Keeling, Brendon Lovett and Niya Petkova for formative discussions.

-
- [1] G. Lerario, D. Ballarini, A. Fieramosca, A. Cannavale, A. Genco, F. Mangione, S. Gambino, L. Dominici, M. De Giorgi, G. Gigli, and D. Sanvitto, *Light Sci. Appl.* **6**, e16212 (2016).
 - [2] S. Hou, M. Khatoniar, K. Ding, Y. Qu, A. Napolov, V. M. Menon, and S. R. Forrest, *Adv. Mater.* **32**, 2002127 (2020).
 - [3] B. Liu, J. Horowitz, and S. R. Forrest, *ACS Photonics* **10**, 4476 (2023).
 - [4] S. Ghosh, R. Su, J. Zhao, A. Fieramosca, J. Wu, T. Li, Q. Zhang, F. Li, Z. Chen, T. Liew, D. Sanvitto, and Q. Xiong, *Photonics Insights* **1**, R04 (2022).
 - [5] G. G. Rozenman, K. Akulov, A. Golombek, and T. Schwartz, *ACS Photonics* **5**, 105 (2018).
 - [6] M. Balasubrahmaniam, A. Simkhovich, A. Golombek, G. Sandik, G. Ankonina, and T. Schwartz, *Nat. Mater.* **22**, 338 (2023).
 - [7] A. M. Berghuis, R. H. Tichauer, L. M. A. Jong, I. Sokolovskii, P. Bai, M. Ramezani, S. Murai, G. Groenhof, and J. Gómez Rivas, *ACS Photonics* **9**, 2263 (2022).
 - [8] A. M. Berghuis, A. Boom, R. P. Argante, S. Murai, and J. Gómez Rivas, *ACS Nano* **18**, 31987 (2024).
 - [9] R. Pandya, R. Y. S. Chen, Q. Gu, J. Sung, C. Schneidermann, O. S. Ojambati, R. Chikkaraddy, J. Gorman, G. Jacucci, O. D. Onelli, T. Willhammar, D. N. Johnstone, S. M. Collins, P. A. Midgley, F. Auras, T. Baikie, R. Jayaprakash, F. Mathevet, R. Soucek, M. Du, A. M. Alvertis, A. Ashoka, S. Vignolini, D. G. Lidzey, J. J. Baumberg, R. H. Friend, T. Barisien, L. Legrand, A. W. Chin, J. Yuen-Zhou, S. K. Saikin, P. Kukura, A. J. Musser, and A. Rao, *Nat. Commun.* **12**, 6519 (2021).
 - [10] R. Pandya, A. Ashoka, K. Georgiou, J. Sung, R. Jayaprakash, S. Renken, L. Gai, Z. Shen, A. Rao, and A. J. Musser, *Adv. Sci.* **9**, 2105569 (2022).
 - [11] D. Xu, A. Mandal, J. M. Baxter, S.-W. Cheng, I. Lee, H. Su, S. Liu, D. R. Reichman, and M. Delor, *Nat. Commun.* **14**, 3881 (2023).

- [12] L. Jin, A. D. Sample, D. Sun, Y. Gao, S. Deng, R. Li, L. Dou, T. W. Odom, and L. Huang, *ACS Photonics* **10**, 1983 (2023).
- [13] S.-W. Cheng, D. Xu, H. Su, J. M. Baxter, L. N. Holtzman, K. Watanabe, T. Taniguchi, J. C. Hone, K. Barkmak, and M. Delor, *Nano Lett.* **23**, 9936 (2023).
- [14] G. Groenhof, C. Climent, J. Feist, D. Morozov, and J. J. Toppari, *J. Phys. Chem. Lett.* **10**, 5476 (2019).
- [15] E. Suyabatmaz and R. F. Ribeiro, *J. Chem. Phys.* **159**, 034701 (2023).
- [16] A. N. Osipov, I. V. Iorsh, A. V. Yulin, and I. A. Shelykh, *Phys. Rev. B* **108**, 104202 (2023).
- [17] I. Sokolovskii, R. H. Tichauer, D. Morozov, J. Feist, and G. Groenhof, *Nat. Commun.* **14**, 6613 (2023).
- [18] R. H. Tichauer, I. Sokolovskii, and G. Groenhof, *Adv. Sci.* **10**, 2302650 (2023).
- [19] I. Tutunnikov, M. Qutubuddin, H. R. Sadeghpour, and J. Cao, *arXiv:2410.11051* (2024).
- [20] Z. Zhou, H.-T. Chen, M. Sukharev, J. E. Subotnik, and A. Nitzan, *Phys. Rev. A* **109**, 033717 (2024).
- [21] W. Ying, B. X. K. Chng, and P. Huo, *arXiv:2411.08288* (2024).
- [22] N. Krupp, G. Groenhof, and O. Vendrell, *arXiv:2410.23739* (2024).
- [23] J. Liu and Y. Yao, *arXiv:2405.16044* (2024).
- [24] L. Blackham, A. Manjalingal, S. R. Koshkaki, and A. Mandal, *arXiv:2501.16622* (2025).
- [25] B. X. K. Chng, M. E. Mondal, W. Ying, and P. Huo, *Nano Lett.* **25**, 1617 (2025).
- [26] T. Khazanov, S. Gunasekaran, A. George, R. Lomlu, S. Mukherjee, and A. J. Musser, *Chem. Phys. Rev.* **4**, 041305 (2023).
- [27] S. R. Koshkaki, A. Manjalingal, L. Blackham, and A. Mandal, *arXiv:2502.12933* (2025).
- [28] S. Renken, R. Pandya, K. Georgiou, R. Jayaprakash, L. Gai, Z. Shen, D. G. Lidzey, A. Rao, and A. J. Musser, *J. Chem. Phys.* **155**, 154701 (2021).
- [29] M. Reitz, A. Koner, and J. Yuen-Zhou, *arXiv:2410.16630* (2024).
- [30] R. H. Tichauer, J. Feist, and G. Groenhof, *J. Chem. Phys.* **154**, 104112 (2021).
- [31] P. Fowler-Wright, *Mean-field and cumulant approaches to modelling organic polariton physics* (2024), PhD Thesis.
- [32] F. Carollo and I. Lesanovsky, *Phys. Rev. Lett.* **126**, 230601 (2021).
- [33] H.-T. Chen, T. E. Li, M. Sukharev, A. Nitzan, and J. E. Subotnik, *J. Chem. Phys.* **150**, 044102 (2019).
- [34] M. A. Zeb, P. G. Kirton, and J. Keeling, *ACS Photonics* **5**, 249 (2018).
- [35] S. Mukamel, *Principles of Nonlinear Optical Spectroscopy*, Oxford Series in Optical and Imaging Sciences (Oxford University Press, New York, 1995).
- [36] J. B. Pérez-Sánchez and J. Yuen-Zhou, *Nature Communications* **16**, 3151 (2025).
- [37] J. B. Pérez-Sánchez, A. Koner, S. Raghavan-Chitra, and J. Yuen-Zhou, *arXiv:2410.14175* (2024).
- [38] K. Schwennicke, A. Koner, J. B. Pérez-Sánchez, W. Xiong, N. C. Giebink, M. L. Weichman, and J. Yuen-Zhou, *arXiv:2408.05036* (2024).
- [39] J. d. Pino, J. Feist, and F. J. Garcia-Vidal, *New Journal of Physics* **17**, 053040 (2015).
- [40] R. F. Ribeiro, L. A. Martínez-Martínez, M. Du, J. Campos-Gonzalez-Angulo, and J. Yuen-Zhou, *Chem. Sci.* **9**, 6325 (2018).
- [41] L. A. Martínez-Martínez, E. Eizner, S. Kéna-Cohen, and J. Yuen-Zhou, *J. Chem. Phys.* **151**, 054106 (2019).
- [42] See Supplemental Material at <http://link.aps.org/supplemental/> for a movie file showing the spatially resolved pump-probe spectra of Fig. 3.
- [43] C. A. DelPo, B. Kudisch, K. H. Park, S.-U.-Z. Khan, F. Fassioli, D. Fausti, B. P. Rand, and G. D. Scholes, *J. Phys. Chem. Lett.* **11**, 2667 (2020).
- [44] A. Strashko, P. Kirton, and J. Keeling, *Phys. Rev. Lett.* **121**, 193601 (2018).
- [45] M. Sánchez-Barquilla, R. E. F. Silva, and J. Feist, *J. Chem. Phys.* **152**, 034108 (2020).
- [46] Q. Zhou, S. A. H. Gangaraj, M. Zhou, and Z. Yu, *arXiv:2410.16118* (2024).
- [47] L. Novotny and B. Hecht, *Principles of Nano-Optics*, 2nd ed. (Cambridge University Press, Cambridge, 2012).
- [48] R. Shankar, *Principles of quantum mechanics*, 2nd ed. (Plenum Press, New York, 1994).
- [49] J. Yuen-Zhou and A. Koner, *J. Chem. Phys.* **160**, 154107 (2024).
- [50] M. A. Zeb, *Phys. Rev. A* **106**, 063720 (2022).

Polaritonic Beer-Lambert law

To obtain an analytical expression for the propagation of photonic modes in the cavity, we linearize the mean-field equations by writing $\langle \sigma_n^z \rangle = z_n^{(0,0)} + \delta z_n$, where $z_n^{(0,0)}$ is time-independent. In a leading-order approximation, we assume that changes to the molecular population are small, $|\delta z_n| \ll |z_n^{(0,0)}|$, such that Eqs. (4a) and (4b) for the photon and coherence expectations form a closed set:

$$\partial_t \langle \tilde{a}_n \rangle = -(i\omega_c + \kappa/2) \langle \tilde{a}_n \rangle - i\Omega \langle \sigma_n^- \rangle + iC \partial_n^2 \langle \tilde{a}_n \rangle, \quad (11a)$$

$$\partial_t \langle \sigma_n^- \rangle = -(i\omega_0 + \gamma_\phi/2) \langle \sigma_n^- \rangle + i\Omega z_n^{(0,0)} \langle \tilde{a}_n \rangle. \quad (11b)$$

For simplicity we set $\langle \tilde{a}_n^{\text{in}} \rangle = 0$, to derive an expression after the driving fields have switched off, but the following is readily generalized to include non-zero input.

Equations (11a) and (11b) can be solved by taking Fourier transforms. Defining $\alpha_n(\omega) = \int dt e^{i\omega t} \langle \tilde{a}_n \rangle(t)$, $s_n(\omega) = \int dt e^{i\omega t} \langle \sigma_n^- \rangle(t)$, we find

$$-i\omega s_n(\omega) = -(i\omega_0 + \gamma_\phi/2) s_n(\omega) + i\Omega z_n^{(0,0)} \alpha_n(\omega) \quad (12)$$

$$\Rightarrow s_n(\omega) = -\Omega \chi(\omega) \alpha_n(\omega), \quad (13)$$

where the molecular susceptibility is defined as

$$\chi(\omega) = \frac{z_n^{(0,0)}}{(\omega - \omega_0) + i\gamma_\phi/2}. \quad (14)$$

For a uniform molecular population (e.g., all molecules in the ground state, $z_n^{(0,0)} \equiv -1$), $\chi(\omega)$ is independent of position n .

Substituting Eq. (13) into the equation for $\alpha_n(\omega)$ yields

$$\begin{aligned} -i\omega\alpha_n(\omega) &= -(i\omega_c + \kappa/2)\alpha_n(\omega) + iC\partial_n^2\alpha_n(\omega) \\ &\quad - i\Omega s_n(\omega) \end{aligned} \quad (15)$$

$$\Rightarrow \partial_n^2\alpha_n(\omega) = \lambda^2(\omega)\alpha_n(\omega), \quad (16)$$

where $\lambda^2(\omega) = -(1/C)[(\omega - \omega_c) + i\kappa/2 + \Omega^2\chi(\omega)]$ relates to the retarded photon Green's function, as described in the Letter.

Equation (16) is a (1D) Helmholtz equation, which arises commonly, e.g., in electromagnetism [47] and quantum scattering problems [48]. It admits two solutions:

$$\alpha_n^{\rightarrow}(\omega) = Ae^{\lambda(\omega)n}, \quad \alpha_n^{\leftarrow}(\omega) = Ae^{-\lambda(\omega)n}, \quad (17)$$

corresponding to right- and left-propagating waves when $\text{Im}\lambda(\omega) > 0$. Accordingly, the real part of the propagation constant, $\text{Re}\lambda(\omega) = \text{Re}[D^R(\omega)]^{-1/2}$ governs the decay of the intracavity field at frequency ω , as expressed in Eq. (6). We note further that, whilst derived for our simplified model comprising two-level systems, this result can be naturally generalized to complex multi-level systems where the susceptibility $\chi(\omega)$ is replaced by the full molecular self-energy [49].

Bright and dark exciton populations

Bright excitonic states are symmetric superpositions of all emitter states that couple to a cavity mode [50]. From the interaction in Eq. (1), we define the bright-state operator for the k^{th} mode as:

$$\sigma_k^+ = \frac{1}{\sqrt{N}} \sum_{n=1}^N e^{-ikr_n} \sigma_n^+. \quad (18)$$

Applying our spatial coarse-graining to N_k positions, we rewrite the sum over all molecules as a sum over positions $r_n = n\Delta r$ ($n = 1, \dots, N_k$) and the N_E molecules at each position:

$$\sigma_k^+ = \frac{1}{\sqrt{N}} \sum_{n=1}^{N_k} \sum_{x=1}^{N_E} e^{-ikr_n} \sigma_{nx}^+. \quad (19)$$

The total bright excitonic population as a function of position is then obtained from

$$p_n^{B\text{-tot}} = \frac{1}{N_k} \sum_{k,k'} \langle \sigma_k^+ \sigma_{k'}^- \rangle e^{i(k'-k)r_n}. \quad (20)$$

When evaluating Eq. (20), care must be taken when calculating coherences $\langle \sigma_{nx}^+ \sigma_{my}^- \rangle$ for $n = m$ and $x = y$, i.e., when the indices refer to the same molecule. In this case, $\langle \sigma_{nx}^+ \sigma_{nx}^- \rangle \equiv (1 + \langle \sigma_{nx}^z \rangle)/2$, and a mean-field approximation should not be applied. With this in mind, from Eq. (20) it follows that

$$p_n^{B\text{-tot}} = (N_E - 1) |\langle \sigma_{nx}^+ \rangle|^2 + \frac{1}{2} (\langle \sigma_{nx}^z \rangle + 1). \quad (21)$$

Since molecules at the same position share identical on-site properties, we write $\langle \sigma_{nx}^+ \rangle = \langle \sigma_n^+ \rangle$, where $\langle \sigma_n^+ \rangle$ is the expectation for any molecule at n . In the large- N limit, where $N_E = N/N_k \gg 1$, we obtain

$$p_n^{B\text{-tot}} \approx |\langle \sigma_n^+ \rangle|^2. \quad (22)$$

The dark state population $p_n^{D\text{-tot}}$ is given by the total molecular population at n , $p_n^{m\text{-tot}} = N_E(1 + \langle \sigma_n^z \rangle)$, minus the bright-state contribution:

$$\begin{aligned} p_n^{D\text{-tot}} &= p_n^{m\text{-tot}} - p_n^{B\text{-tot}} \\ &\approx N_E [(1 + \langle \sigma_n^z \rangle)/2 - |\langle \sigma_n^+ \rangle|^2]. \end{aligned} \quad (23)$$

Equations (8a) and (8b) for the dynamics of the scaled populations $p_n^B = p_n^{B\text{-tot}}/N_E$ and $p_n^D = p_n^{D\text{-tot}}/N_E$ follow straightforwardly from the mean-field Eqs. (4b) and (4c) for $\langle \sigma_n^- \rangle$ and $\langle \sigma_n^z \rangle$.

Perturbative pump-probe equations

As explained in the Letter, the leading contribution to the nonlinear differential transmission ΔT_n arises from terms second order in the pump and first order in the probe [29]: $\alpha_n^{(0,1)}$ and $\alpha_n^{(2,1)}$. The equations of motion for variables at a given order depend on those of equal or lower order. Thus, in principle, one requires the dynamics of all $\alpha_n^{(a,b)}$, $\sigma_n^{(a,b)}$, and $z_n^{(a,b)}$ for $a \leq 2$, $b \leq 1$.

However, many of these variables remain trivial for the initial conditions we consider, $\langle \tilde{a}_n \rangle = \langle \sigma_n^- \rangle = 0$, $\langle \sigma_n^z \rangle = -1$ at $t = 0$. This ensures all $\alpha_n^{(a,b)}$, $\sigma_n^{(a,b)}$, and $z_n^{(a,b)}$ are initially zero, except for $z_n^{(0,0)} \equiv -1$. The resulting nontrivial set of equations is:

$$\begin{aligned}
\partial_t \alpha_n^{(1,0)} &= - (i\omega_c + \kappa/2 - iC\partial_n^2) \alpha_n^{(1,0)} - i\Omega \sigma_n^{(1,0)} + D_n^p f_p(t) e^{-i\omega_p t}, \\
\partial_t \sigma_n^{(1,0)} &= -(i\omega_0 + \gamma_\phi/2) \sigma_n^{(1,0)} + i\Omega z_n^{(0,0)} \alpha_n^{(1,0)}, \\
\partial_t z_n^{(2,0)} &= -4\Omega \text{Im} \left[\sigma_n^{(1,0)} \bar{\alpha}_n^{(1,0)} \right], \\
\partial_t \alpha_n^{(0,1)} &= - (i\omega_c + \kappa/2 - iC\partial_n^2) \alpha_n^{(0,1)} - i\Omega \sigma_n^{(0,1)} + D_n^{p'} f_{p'}(t) e^{-i\omega_{p'} t}, \\
\partial_t \sigma_n^{(0,1)} &= -(i\omega_0 + \gamma_\phi/2) \sigma_n^{(0,1)} + i\Omega z_n^{(0,0)} \alpha_n^{(0,1)}, \\
\partial_t z_n^{(1,1)} &= -4\Omega \text{Im} \left[\sigma_n^{(1,0)} \bar{\alpha}_n^{(0,1)} + \sigma_n^{(0,1)} \bar{\alpha}_n^{(1,0)} \right], \\
\partial_t \alpha_n^{(2,1)} &= - (i\omega_c + \kappa/2 - iC\partial_n^2) \alpha_n^{(2,1)} - i\Omega \sigma_n^{(2,1)}, \\
\partial_t \sigma_n^{(2,1)} &= -(i\omega_0 + \gamma_\phi/2) \sigma_n^{(2,1)} + i\Omega \left(z_n^{(0,0)} \alpha_n^{(2,1)} + z_n^{(1,1)} \alpha_n^{(1,0)} + z_n^{(2,0)} \alpha_n^{(0,1)} \right).
\end{aligned} \tag{24}$$

Here, we have explicitly included the pump and probe driving terms from Eq. (5). As in the Letter, an overbar is used to denote a complex conjugate. These equations were obtained by first deriving the Heisenberg equations of motion for the single-operator expectations $\langle \tilde{a}_n \rangle$, $\langle \sigma_n^- \rangle$, and $\langle \sigma_n^z \rangle$ from the master equation (3). The mean-field approximation, $\langle \tilde{a}_n \sigma_n^z \rangle \approx \langle \tilde{a}_n \rangle \langle \sigma_n^z \rangle$, $\langle \tilde{a}_n \sigma_n^+ \rangle \approx \langle \tilde{a}_n \rangle \langle \sigma_n^+ \rangle$, was applied before making the expansion described by Eq. (9) and collecting terms of identical order in η_p and $\eta_{p'}$.